

Activity-induced droplet propulsion and multifractality

Nadia Bihari Padhan^{1,*} and Rahul Pandit^{1,†}

¹*Centre for Condensed Matter Theory, Department of Physics,
Indian Institute of Science, Bangalore 560012, India*

(Dated: September 13, 2022)

We develop a minimal hydrodynamic model, without an orientational order parameter, for assemblies of contractile swimmers encapsulated in a droplet of a binary-fluid emulsion. Our model uses two coupled scalar order parameters, ϕ and ψ , which capture, respectively, the droplet interface and the activity of the contractile swimmers inside this droplet. These order parameters are also coupled to the velocity field \mathbf{u} . At low activity, our model yields a self-propelling droplet whose center of mass (CM) displays rectilinear motion, powered by the spatiotemporal evolution of the field ψ , which leads to a time-dependent vortex dipole at one end of the droplet. As we increase the activity, this CM shows chaotic super-diffusive motion, which we characterize by its mean-square displacement; and the droplet interface exhibits multifractal fluctuations, whose spectrum of exponents we calculate. We explore the implications of our results for experiments on active droplets of contractile swimmers.

I. INTRODUCTION

Active matter comprises systems that are far from equilibrium and in which the constituents extract energy from their surroundings, do mechanical work, and dissipate energy to the same environment [1–4]. The self-organisation of the constituents of such systems can lead to large-scale pattern formation, observed in, e.g., crowds [5, 6], fish schools [7], bird flocks [8, 9], and bacterial colonies [10]. They exhibit a variety of fascinating emergent phenomena, e.g., Motility-Induced-Phase-Separation (MIPS), in which an initially uniform state of active swimmers separates spontaneously into dense and dilute phases, driven by persistent motion and repulsion [11–13]. Most experiments, with motile bacteria or synthetic micro-swimmers, use confinement – solid immovable or soft, e.g., by a droplet boundary – that plays a crucial role in the spatiotemporal patterns in assemblies of active micro-swimmers [14–16]. Certain bacterial systems, when confined to a droplet, can propel and deform the droplet [16–18]; self-propelling, or *active* droplets have been considered in nematic-like ordered, active-polar, chemically driven, and phase-field systems [19–27].

We develop a *minimal phase-field model* for assemblies of *contractile swimmers* encapsulated in a droplet of a binary-fluid emulsion, to obtain self-propelling droplets, which are powered by the rich spatio-temporal dynamics of the contractile-swimmer field; this propulsion does not require any orientational ordering. Our results are of direct relevance to active droplets of contractile swimmers

such as *Chlamydomonas reinhardtii* [28, 29] (*C. reinhardtii*). Our phase-field theory has two conserved scalar order parameters ϕ and ψ . The former distinguishes between two, coexisting liquid phases, separated by an interface at the droplet boundary; the latter is related to the bacterial concentration; ϕ and ψ are coupled to each other and to the flow velocity \mathbf{u} , as in the Cahn-Hilliard-Navier-Stokes (CHNS) system or model H [30, 31]. In the absence of the direct coupling between the two order parameters, our model decouples into (a) the CHNS model, for ϕ and \mathbf{u} , that has been used to study multifractal droplet dynamics [30] in a turbulent flow and (b) the *active model H*, for ψ and \mathbf{u} , that has been used to study MIPS [11, 32, 33].

We carry out pseudospectral direct numerical simulations (DNSs) of our model to uncover the dependence of the spatiotemporal evolution of an emergent active droplet on the *activity* parameter A (defined below). For low values of A , the center-of-mass (CM) of the droplet shows rectilinear motion, associated with a time-dependent vortex dipole at one of its ends; as A increases, the droplet fluctuates and its CM exhibits a crossover from rectilinear to super-diffusive motion, reminiscent of Lévy walks. Furthermore, at large values of A , the bacterial field generates low-Reynolds-number, but turbulent, flows and *multifractal deformation* of the active-droplet boundary.

II. MODEL

We use the free-energy functional

$$\mathcal{F}[\phi, \nabla\phi, \psi, \nabla\psi] = \int_{\Omega} \left(\frac{3}{16} \left(\frac{\sigma_1}{\epsilon_1} (\phi^2 - 1)^2 + \frac{\sigma_2}{\epsilon_2} (\psi^2 - 1)^2 \right) - \beta\phi\psi + \frac{3}{4} (\sigma_1\epsilon_1 |\nabla\phi|^2 + \sigma_2\epsilon_2 |\nabla\psi|^2) \right) d\Omega, \quad (1)$$

* nadia@iisc.ac.in

† rahul@iisc.ac.in

where Ω is the region we consider, σ_1 and σ_2 are surface-tension coefficients, ϵ_1 and ϵ_2 are widths of the ϕ and ψ interfaces, respectively, and the attractive coupling $\beta > 0$. To address experiments on active droplets carried out under planar confinement we use the following 2D *active* CHNS equations:

$$\partial_t \phi + (\mathbf{u} \cdot \nabla) \phi = M_1 \nabla^2 \left(\frac{\delta \mathcal{F}}{\delta \phi} \right); \quad (2)$$

$$\partial_t \psi + (\mathbf{u} \cdot \nabla) \psi = M_2 \nabla^2 \left(\frac{\delta \mathcal{F}}{\delta \psi} \right); \quad (3)$$

$$\partial_t \omega + (\mathbf{u} \cdot \nabla) \omega = \nu \nabla^2 \omega - \alpha \omega + [\nabla \times (\mathfrak{S}^\phi + \mathfrak{S}^\psi)]; \quad (4)$$

$$\nabla \cdot \mathbf{u} = 0; \quad \omega = (\nabla \times \mathbf{u}); \quad (5)$$

$$\mathfrak{S}^\phi = -(3/2)\sigma_1\epsilon_1\nabla^2\phi\nabla\phi; \quad (6)$$

$$\mathfrak{S}^\psi = -(3/2)\tilde{\sigma}_2\epsilon_2\nabla^2\psi\nabla\psi; \quad (7)$$

the constant fluid density $\rho = 1$, the advection-diffusion equations (2) and (3) use the constant mobilities M_1 and M_2 for ϕ and ψ , respectively, and the 2D incompressible Navier-Stokes equations (4) and (5) use the vorticity ω , the kinematic viscosity ν , and the bottom friction α ; the interfacial stress \mathfrak{S}^ϕ [Eq. (6)] from ϕ and is derived from \mathcal{F} ; for the *active stress* \mathfrak{S}^ψ [Eq. (7)] from ψ we use the active-model-H formulation for MIPS [11, 32, 33]; both ω and $[\nabla \times (\mathfrak{S}^\phi + \mathfrak{S}^\psi)]$ lie normal to the 2D plane. We refer to ψ as the active scalar [34]. Note that the mechanical surface tension $\tilde{\sigma}_2 \neq \sigma_2$; and $\tilde{\sigma}_2$ can take both negative and positive values unlike σ_1 and σ_2 , which are always positive. For contractile (extensible) swimmers $\tilde{\sigma}_2 < 0$ ($\tilde{\sigma}_2 > 0$) and the system shows arrested phase separation (complete phase separation) [32]. The spatiotemporal evolution of the fields in Eqs. (1)-(7) depend on the initial conditions (see below) and the non-dimensional Cahn numbers $\text{Cn}_1 = \epsilon_1/R_0$ and $\text{Cn}_2 = \epsilon_2/R_0$, Weber numbers $\text{We}_1 = R_0U_0^2/\sigma_1$ and $\text{We}_2 = R_0U_0^2/\sigma_2$, Peclet numbers $\text{Pe}_1 = R_0U_0\epsilon_1/(M_1\sigma_1)$ and $\text{Pe}_2 = R_0U_0\epsilon_2/(M_2\sigma_2)$, order-parameter couplings $\beta'_1 = \beta\epsilon_1/\sigma_1$ and $\beta'_2 = \beta\epsilon_2/\sigma_2$, friction $\alpha' = \alpha R_0/U_0$, Reynolds number $\text{Re} = R_0U_0/\nu$, where $U_0 = \langle U_{CM}(t) \rangle_t$, with U_{CM} the speed of the droplet's center of mass (*CM*) (see below and Appendix B), and, most important, the *activity*

$$A = |\tilde{\sigma}_2|/\sigma_2; \quad (8)$$

we concentrate on contractile swimmers with $\tilde{\sigma}_2 < 0$. In Table-I of Appendix B we list the parameters for our DNS runs R1-R7.

III. INITIAL CONDITIONS AND NUMERICAL METHODS

We consider an initially stationary and circular droplet, of radius R_0 and with its center at $(x_{0,1}, x_{0,2}) =$

(π, π) :

$$\mathbf{u}(\mathbf{x}, t = 0) = 0;$$

$$\phi(\mathbf{x}, t = 0) = \tanh \left(\frac{R_0 - \sqrt{(x_1 - x_{0,1})^2 + (x_2 - x_{0,2})^2}}{\epsilon_1} \right);$$

$$\psi(\mathbf{x}, t = 0) = \begin{cases} \psi_0(\mathbf{x}) & \text{for } |\mathbf{x}| \leq R_0; \\ -1 & \text{for } |\mathbf{x}| > R_0; \end{cases} \quad (9)$$

$\psi_0(\mathbf{x})$ is a random number distributed uniformly on the interval $[-0.1, 0.1]$. Regions with negative (positive) values of ϕ and ψ have low (high) densities of these scalars.

Our DNS of Eqs. (1)-(7) employs a standard Fourier pseudospectral method [35], with the 1/2 rule for the removal of aliasing errors. We use a square domain of side $L = 2\pi$, with period boundary conditions in both spatial directions, and N^2 collocation points. For time integration, we use the semi-implicit ETDRK-2 method [36]. Our computer program is written in CUDA C and is optimised for recent GPU architectures, such as the one used in the NVIDIA A100 processor.

IV. SPATIOTEMPORAL EVOLUTION

To monitor the spatiotemporal evolution of the initial droplet [Eq. (9)] we obtain pseudocolor plots of ϕ and ψ (Fig. 1) and we compute

$$\begin{aligned} U_{CM}(t) &= \sqrt{\sum_{i=1}^2 \left[\sum_{\mathbf{x} \ni \phi(\mathbf{x}, t) > 0} u_i(\mathbf{x}, t) \right]^2}, \\ E(k, t) &= \frac{1}{2} \sum_{k-1/2 < k' < k+1/2} [\hat{\mathbf{u}}(\mathbf{k}', t) \cdot \hat{\mathbf{u}}(-\mathbf{k}', t)], \\ S_\psi(k, t) &= \sum_{k-1/2 < k' < k+1/2} |\hat{\psi}(\mathbf{k}', t)|^2, \\ S_\phi(k, t) &= \sum_{k-1/2 < k' < k+1/2} |\hat{\phi}(\mathbf{k}', t)|^2, \\ \mathcal{L}(t) &= 2\pi \sum_k S_\psi(k, t) / \sum_k k S_\psi(k, t), \\ \mathcal{M}(t) &= \left\langle \sum_{i=1}^2 (x_{CM,i}(t) - x_{CM,i}(t_0))^2 \right\rangle, \\ \Gamma(t) &= [\mathcal{S}(t)/\mathcal{S}_0(t)] - 1, \end{aligned} \quad (10)$$

which are, respectively, the speed of the droplet's *CM*, the fluid energy spectrum, the spectra of ψ and ϕ , a length scale that follows from S_ψ , the mean-square displacement of the droplet's *CM*, and the normalised perimeter of the $\phi = 0$ contour that bounds the droplet [$\mathcal{S}(t)$ is the perimeter of the droplet at time t and $\mathcal{S}_0(t)$ is the perimeter of a circular droplet of equal area at time t]; the subscripts i and *CM* denote Cartesian components and the droplet's *CM*, respectively; carets indicate spatial Fourier transform; and k and k' are the moduli of

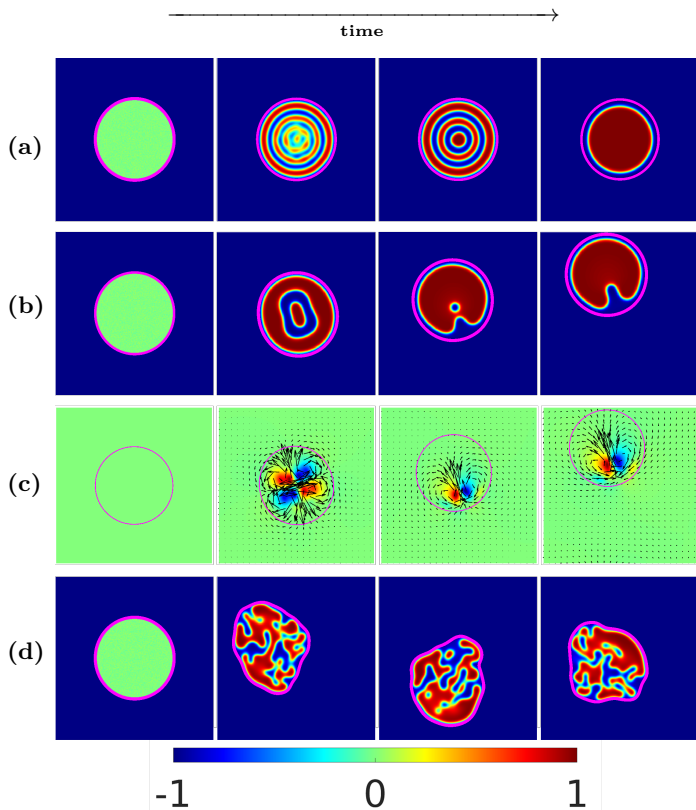


FIG. 1. Illustrative pseudocolor plots of ψ , with the $\phi = 0$ contour shown in magenta, at different representative times (increasing from left to right) for (a) $A = 0$ (no droplet propulsion), (b) $A = 0.15$ (rectilinear droplet propulsion), and (d) $A = 1$ (turbulent droplet propulsion). In (c) we show, for $A = 0.15$, vector plots of the velocity field \mathbf{u} , with the $\phi = 0$ contour line (magenta), overlaid on a pseudocolor plot of the vorticity ω normalised by its maximal value; the lengths of velocity vectors are proportional to their magnitudes. [See videos V1, V2, V3, and V4, in Appendix E.]

the wave vectors \mathbf{k} and \mathbf{k}' . In Fig. 1 we illustrate the evolution of the initial droplet [Eq. (9)] via pseudocolor plots of ψ and the $\phi = 0$ contour (in magenta), at different representative times and $A = 0$ [row (a)], $A = 0.15$ [row (b)], and $A = 1$ [row (d)]; in row (c) we show, for $A = 0.15$, vector plots of the velocity field \mathbf{u} , with the $\phi = 0$ contour line, overlaid on a pseudocolor plot of the vorticity ω normalised by its maximal value. Case $A = 0$ [row (a)]: there is no mean flow, i.e., $U_{CM}(t) = 0$ for all t ; however, as time increase (from left to right), the initially homogeneous mixture of active matter becomes unstable and undergoes phase separation via the formation of self-organized alternating rings of regions with positive and negative values of ψ (cf. oil-water phase separation in a microfluidic droplet [37]); eventually, complete phase separation occurs, via successive ring collapses, and we obtain a $\psi > 0$ region (red) surrounded by a $\psi < 0$ ring (blue) inside the $\phi = 0$ contour.

As we increase A , we find a remarkable transition to a

self-propelling droplet, whose motion we depict, for the illustrative value $A = 0.15$, via pseudocolor plots in Figs. 1(b) and the video V2 in Appendix E. Initially, phase separation tries to set in, but is partially arrested; at this stage the flow field is dominated by a vortex quadrupole [second panels in Figs. 1(b) and (c)]; thereafter, an umbilicus, which forms at one end of the droplet, oscillates periodically in time as it shoots out a tiny blue bead, with $\psi < 0$ [third and fourth panels in Fig. 1(b)]; the associated flow patterns contain an oscillating vortex dipole [third and fourth panels in Fig. 1 (c) and the video V3 in E] that propels the droplet along a straight line [the orange trajectory in Fig. 2 (b)] [38]. These oscillations are mirrored in the periodic time dependence of $\mathcal{L}(t)/R_0$ [magenta curve in Fig. 2 (a)] and $U_{CM}(t)$ [magenta curve in Fig. 3 (a)] and also in a limit cycle whose projection can be viewed in the $\mathcal{L}(t) - U_{CM}(t)$ plane [magenta curve in Fig. 4 (a) in Appendix B]. Thus, as we increase A , the initial transition from a static to a self-propelling droplet can be associated with the formation of a stable limit cycle.

For sufficiently large A ($\gtrsim 0.5$), statistically steady *active-fluid turbulence* develops inside the droplet and leads to important modifications in its structure and propulsion: (a) We find a significant suppression of the phase separation of the active scalar [Figs. 1(d)], which is reminiscent of turbulence-induced coarsening arrest in a binary-fluid mixture [31]; (b) chaotic temporal fluctuations in $\mathcal{L}(t)/R_0$ [Fig. 2 (a)]; (c) convoluted trajectories in the CM of the droplet [e.g., the blue-purple trajectory in Fig. 2 (b)], which are accompanied by chaotic temporal fluctuations in $U_{CM}(t)$ [Fig. 3 (a)], and the projections of the phase-space trajectories in the $\mathcal{L}(t) - U_{CM}(t)$ plane [red and green curves in Fig. 4 (a) in Appendix B]; (d) multifractal fluctuations of $\Gamma(t)$ [Figs. 3 (d)-(f)]; (e) the energy, ϕ , and ψ spectra that extend over a large range of the wave number k [Figs. 5 (a)-(c) in Appendix B].

The transition from rectilinear to chaotic-droplet trajectories is apparent in the illustrative plots of droplet- CM paths, for $A = 0.15$ (orange) and $A = 1$ (blue-purple) in Fig. 2 (b), which we compute as in Ref. [39] (see Appendix D). From such paths we obtain the normalised mean-square-displacement $\mathcal{M}(t)/R_0^2$, which we present in log-log plots versus the non-dimensional time t in Fig. 2 (c): rectilinear droplet motion leads to $\mathcal{M}(t) \sim t^2$ (red curve for $A = 0.15$). As we increase A , we obtain crossovers to super-diffusive behaviors, which are consistent with $\mathcal{M}(t) \sim t^{5/3}$ (green curve for $A = 0.5$) and $\mathcal{M}(t) \sim t^{4/3}$ (magenta curve for $A = 2$), which suggest Lévy walks for the droplet's CM (cf. the motion of Lagrangian tracers in 2D turbulence and in a model for bacterial turbulence [40, 41]). The activity-induced transition from rectilinear-to-chaotic droplet motion is also mirrored in the time-dependence of $U_{CM}(t)/U_0$ that we depict in Fig. 3(a): the oscillatory behavior at $A = 0.15$ (magenta curve) gives way to chaotic times series as we move from $A = 0.5$ (green) to $A = 1$ (blue). We characterize these chaotic fluctuations by computing the

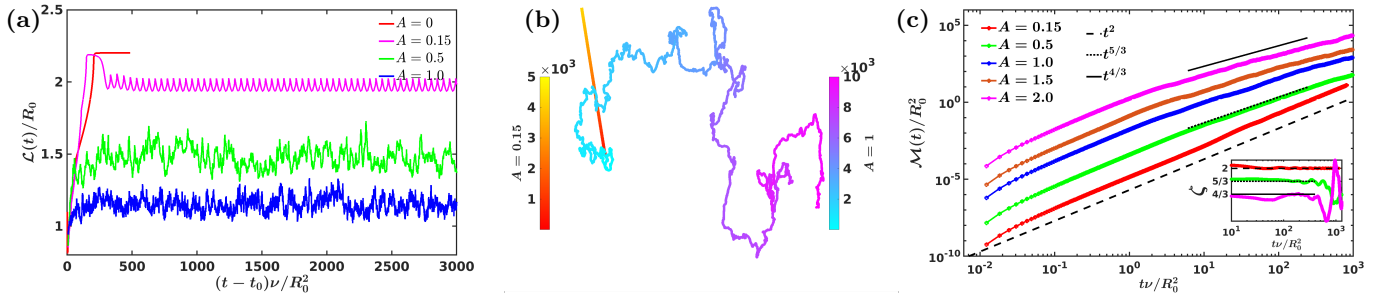


FIG. 2. (a) Plots of $\mathcal{L}(t)/R_0$ [Eq. (10)] versus $(t - t_0)\nu/R_0^2$ for $A = 0$ (red curve), $A = 0.15$ (magenta curve), $A = 0.5$ (green curve), and $A = 1$ (blue curve), with t_0 is a non-universal offset that depends on A . (b) Illustrative trajectories of the droplet's CM for $A = 0.15$ (orange) and $A = 1$ (blue-purple), with colorbars indicating the simulation time. (c) Log-log plots of the mean-square-displacement $\mathcal{M}(t)$ versus $t\nu/R_0^2$ (after the removal of initial transients) for droplet-CM trajectories: $A = 0.15$ (red), $A = 0.5$ (green), $A = 1$ (blue), $A = 1.5$ (dark orange), and $A = 2$ (magenta); initially these plots show ballistic regimes, but, at large times, we see $\mathcal{M}(t) \sim t^\zeta$, with $\zeta = 2$ (rectilinear motion for $A = 0.15$), and superdiffusive regimes with $\zeta = 1.67 \pm 0.02 \simeq 5/3$ (for $A = 0.5$) and $\zeta = 1.28 \pm 0.05 \simeq 4/3$ (for $A = 2$) via local-slope analysis (the inset shows plots of ζ versus t); plots for different values of A are displaced vertically for ease of visualization.

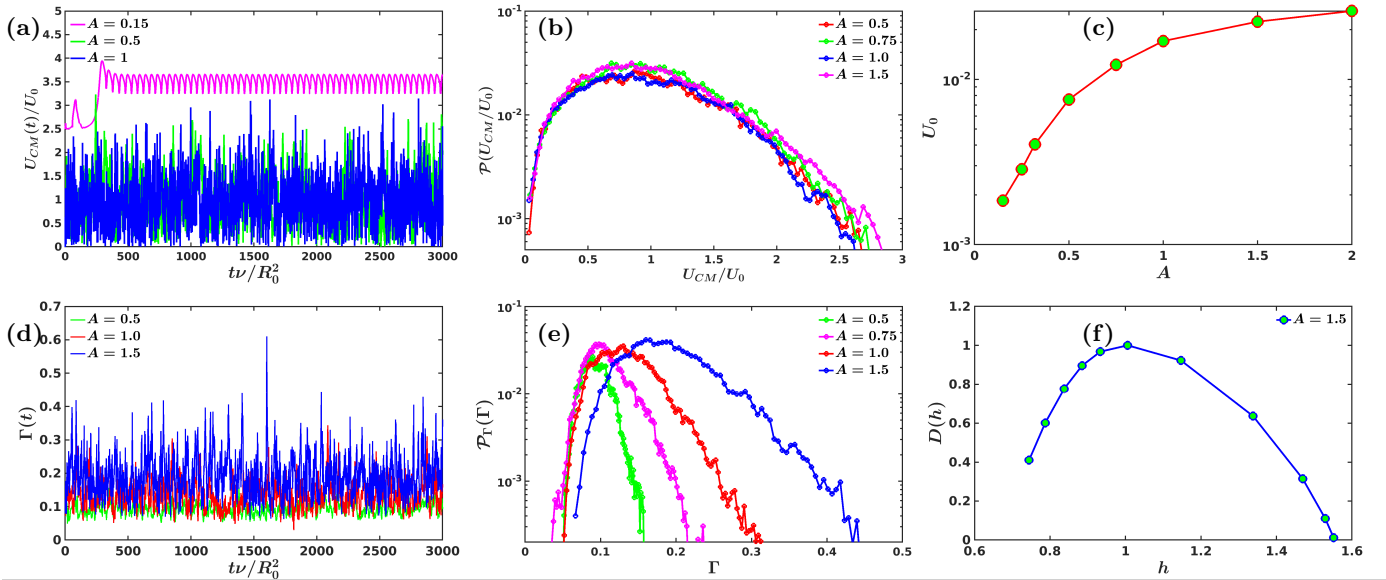


FIG. 3. (a) Plots versus the non-dimensionalized time $t\nu/R_0^2$ of the scaled droplet-CM speed U_{CM}/U_0 [Eq. (10)] for $A = 0.15$ (magenta curve, which has been moved up to aid visualization), $A = 0.5$ (green) and $A = 1$ (blue). (b) Semilog plots of the PDF $\mathcal{P}(U_{CM}/U_0)$ for $A = 0.5$ (red), $A = 0.75$ (green), $A = 1$ (blue), and $A = 1.5$ (magenta). (c) Semilog plot of U_0 versus A . (d) Plots versus $t\nu/R_0^2$ of the normalised droplet perimeter $\Gamma(t)$ [Eq. (10)] for $A = 0.5$ (green), $A = 1$ (red), and $A = 1.5$ (blue). (e) Semilog plots of the PDF of $\mathcal{P}_\Gamma(\Gamma)$ for $A = 0.5$ (green), $A = 0.75$ (magenta), $A = 1$ (red), and $A = 1.5$ (blue). (f) Plots of the multifractal $D(h)$ versus the Hurst exponent h (see text), obtained from $\Gamma(t)$, for $A = 1.5$.

PDF $\mathcal{P}(U_{CM}/U_0)$, which we show in the semi-log plots of Fig. 3(b); these PDFs collapse onto each other, for different values of A , because we use the scaled speed U_{CM}/U_0 ; if we use the unscaled U_{CM} , then the skewness of this PDF increases with A (Fig. 4 (c) in Appendix B). Furthermore, U_0 increases monotonically with A [Fig. 3 (c)] and shows signs of saturation at large A .

Not only does the active droplet display an increase in U_0 with A , but it also exhibits, as A increases, an enhancement in fluctuations in its normalised perimeter $\Gamma(t)$ [Eq. (10)], which we plot versus $t\nu/R_0^2$ in Fig. 3 (d).

These fluctuations of Γ lead to broad PDFs, $\mathcal{P}_\Gamma(\Gamma)$, which we present in Fig. 3 (e), for $A = 0.5$ (green), $A = 0.75$ (magenta), $A = 1$ (red), and $A = 1.5$ (blue); the widths and skewnesses of these PDFs increase with A (see Appendix B). From a multifractal analysis of the time series $\Gamma(t)$, we obtain the generalised spectrum of dimensions $D(h)$ as a function of the Hurst exponent h by using the wavelet-leader method (see Refs. [42, 43] and Appendix C). In Fig. 3 (f) we present an illustrative plot of the multifractal spectrum $D(h)$ for $A = 1.5$ (blue curve). Such multifractality has not been obtained heretofore

for active droplets; it is akin to the recently discovered droplet-perimeter fluctuations in turbulent binary-fluid flows [30].

As the activity induces turbulence in the ψ field, the droplet's motion yields fluid turbulence, which we characterize by the energy, ϕ , and ψ spectra $E(k, t)$, $S_\phi(k, t)$, and $S_\psi(k, t)$ [Eq. (10)], that we plot in Figs. 5(a)-(c) of Appendix B for $A = 0.5$, 1 , and $A = 1.5$. Even though the Reynolds numbers are small, these spectra span several decades in k , a clear signature of turbulence. We will present elsewhere [44] a detailed study of the properties of a statistically homogeneous and isotropic form of this turbulence, which is reminiscent of bacterial or active-fluid turbulence [41, 45, 46] and elastic turbulence in polymer solutions [47, 48].

V. CONCLUSION

We have developed a minimal model for assemblies of contractile swimmers, without alignment interactions, encapsulated in a droplet of a binary-fluid emulsion. Our hydrodynamic model, with the scalar order parameter ϕ and the active scalar ψ coupled to each other and the velocity field \mathbf{u} , not only captures the droplet interface (via the $\phi = 0$ contour) and its fluctuations, but also

leads to droplet self-propulsion, which is rectilinear at low A ($\simeq 0.15$) and chaotic for large values of A , at which the CM of the droplet shows super-diffusive motion and the droplet interface exhibits multifractal fluctuations. Our study is distinct from earlier theoretical studies of active droplets that consider cell-level models in nematically ordered, active polar, chemically driven, or phase-field systems [19–23, 25–27]. By contrast, the activity-induced droplet propulsion in our model arises from the interplay of ϕ , \mathbf{u} , and a collection of contractile swimmers, which are described via the field ψ and are enclosed inside the droplet; this propulsion shows a hitherto unexplored crossover from rectilinear to superdiffusive motion of the droplet CM . We look forward to the experimental verification of our results, especially in active droplets of contractile swimmers such as *C. reinhardtii* [28, 29], where it should be possible to control the activity by changing the oxygen concentration in low-light conditions.

ACKNOWLEDGMENTS

We thank J.K. Alageshan, K.V. Kiran, S.J. Kole, and S. Ramaswamy for discussions, the National Supercomputing Mission (NSM), and SERB (India) for support, and SERC (IISc) for computational resources.

Appendix A: Cahn-Hilliard formalism

It is convenient to write the Cahn-Hilliard free-energy functional for a binary-fluid mixture in the following way:

$$\mathcal{F}(\phi) = \int_{\Omega} \left[\frac{3}{16} \frac{\sigma}{\epsilon} (\phi^2 - 1)^2 + \frac{3}{4} \sigma \epsilon |\nabla \phi|^2 \right]; \quad (\text{A1})$$

this depends on two important physical parameters: σ , the surface tension coefficient, and ϵ , the interface width. The first term is a double-well potential with two minima at $\phi = \pm 1$. The equilibrium interfacial profile $\phi_0(x)$ can be computed by solving the following boundary value problem (if ϕ is assumed to vary along one spatial direction, say x):

$$\begin{cases} \mu(x) = -\frac{3}{2} \sigma \epsilon \frac{d^2 \phi_0}{dx^2} + \frac{3}{4} \frac{\sigma}{\epsilon} (\phi_0^3 - \phi_0) = 0; \\ \lim_{x \rightarrow \pm \infty} \phi_0 = \pm 1. \end{cases} \quad (\text{A2})$$

Here, $\mu(x) \equiv \frac{\delta \mathcal{F}}{\delta \phi}$ is the chemical potential. The solution is

$$\phi_0(x) = \tanh \left(\frac{x - x_0}{\epsilon} \right), \quad (\text{A3})$$

where x_0 is the midpoint of the interface. The interfacial free-energy is

$$\int_{-\infty}^{\infty} \mathcal{F}(\phi_0) dx = \sigma. \quad (\text{A4})$$

The advantage of writing the free-energy functional in the above form is that σ and ϵ can be varied independently of each other. In our direct numerical simulations, we tune the value of ϵ , depending upon the computational mesh size, without changing the surface tension σ .

The stress terms: In the passive CHNS or model-H equations, the stress in the Navier-Stokes equations is

$$\begin{aligned}\mathfrak{S}^\phi &= -\phi\nabla\mu = \mu\nabla\phi - \nabla(\phi\mu) \\ &= -\frac{3}{2}\sigma\epsilon\nabla^2\phi\nabla\phi - \nabla\left(\phi\mu - \frac{3}{4}\frac{\sigma}{\epsilon}(\phi^4/4 - \phi^2/2)\right).\end{aligned}\quad (\text{A5})$$

The second term on the right-hand side of the above equation vanishes when we take the curl to obtain the vorticity equation, so we use the stress $\mathfrak{S}^\phi = -(3/2)\sigma\epsilon\nabla^2\phi\nabla\phi$. There is an alternative way of writing this stress, in terms of a stress tensor, as follows:

$$\begin{aligned}\mathfrak{S}^\phi &= \nabla \cdot \Sigma^\phi = -(3/2)\sigma\epsilon\nabla^2\phi\nabla\phi; \\ \Sigma_{ij}^\phi &= -(3/2)\sigma\epsilon [(\partial_i\phi)(\partial_j\phi) - |\nabla\phi|^2\delta_{ij}/2].\end{aligned}\quad (\text{A6})$$

Similarly, for the stress terms in our active CHNS model, in the main paper, we use:

$$\mathfrak{S}^\phi = -(3/2)\sigma_1\epsilon_1\nabla^2\phi\nabla\phi; \quad (\text{A7})$$

$$\mathfrak{S}^\psi = -(3/2)\tilde{\sigma}_2\epsilon_2\nabla^2\psi\nabla\psi. \quad (\text{A8})$$

Appendix B: Non-dimensional forms

We write the non-dimensionalized forms of Eqs. (1)-(7), in the main paper, by using the following transformations:

$$\mathbf{x}^* = \mathbf{x}/R_0; \quad \mathbf{u}^* = \mathbf{u}/U_0; \quad t^* = tU_0/R_0; \quad \omega^* = \omega U_0/R_0. \quad (\text{B1})$$

The non-dimensionalized equations are (we drop the superscript * to simplify the notations):

$$\partial_t\omega + (\mathbf{u} \cdot \nabla)\omega = \frac{1}{\text{Re}}\nabla^2\omega - \alpha'\omega - \frac{3}{2}\frac{\text{Cn}_1}{\text{We}_1}[\nabla \times (\nabla^2\phi\nabla\phi)] - \frac{3}{2}\frac{\text{ACn}_2}{\text{We}_2}[\nabla \times (\nabla^2\psi\nabla\psi)]; \quad (\text{B2})$$

$$\partial_t\phi + (\mathbf{u} \cdot \nabla)\phi = \frac{3}{2\text{Pe}_1}\nabla^2\left[-\text{Cn}_1^2\nabla^2\phi + \frac{1}{2}(\phi^3 - \phi) - \frac{2}{3}\beta'_1\psi\right]; \quad (\text{B3})$$

$$\partial_t\psi + (\mathbf{u} \cdot \nabla)\psi = \frac{3}{2\text{Pe}_2}\nabla^2\left[-\text{Cn}_2^2\nabla^2\psi + \frac{1}{2}(\psi^3 - \psi) - \frac{2}{3}\beta'_2\phi\right]. \quad (\text{B4})$$

The important *non-dimensional numbers* are:

$$\begin{aligned}\text{the Reynolds number: } \text{Re} &= R_0U_0/\nu; \\ \text{the non-dimensionalized friction: } \alpha' &= \alpha R_0/U_0; \\ \text{Cahn numbers: } \text{Cn}_1 &= \epsilon_1/R_0; \text{Cn}_2 = \epsilon_2/R_0; \\ \text{Weber numbers: } \text{We}_1 &= R_0U_0^2/\sigma_1; \text{We}_2 = R_0U_0^2/\sigma_2; \\ \text{Activity parameter: } \text{A} &= |\tilde{\sigma}_2|/\sigma_2; \\ \text{Order-parameter couplings: } \beta'_1 &= \beta\epsilon_1/\sigma_1; \beta'_2 = \beta\epsilon_2/\sigma_2; \\ \text{Peclet numbers. } \text{Pe}_1 &= \frac{R_0U_0\epsilon_1}{M_1\sigma_1}; \text{Pe}_2 = \frac{R_0U_0\epsilon_2}{M_2\sigma_2}.\end{aligned}\quad (\text{B5})$$

| Run | A | Re | α' | $\text{We}_1 = \text{We}_2$ | $\text{Pe}_1 = \text{Pe}_2$ |
|-----|------|-------|-----------|-----------------------------|-----------------------------|
| R1 | 0 | 0 | ∞ | 0 | 0 |
| R2 | 0.15 | 0.002 | 85 | $\mathcal{O}(10^{-6})$ | 0.1 |
| R3 | 0.5 | 0.008 | 20 | $\mathcal{O}(10^{-5})$ | 0.4 |
| R4 | 0.75 | 0.013 | 13 | $\mathcal{O}(10^{-4})$ | 0.7 |
| R5 | 1.0 | 0.018 | 9 | $\mathcal{O}(10^{-4})$ | 1.0 |
| R6 | 1.5 | 0.02 | 7 | $\mathcal{O}(10^{-4})$ | 1.3 |
| R7 | 2 | 0.03 | 6 | $\mathcal{O}(10^{-3})$ | 1.5 |

TABLE I. The values of various non-dimensional parameters in our DNS Runs R1-R7. The following parameters are fixed in all these runs: $N = 512$, grid size, $dx = 2\pi/N$, $R_0 = \pi/2$, $\text{Cn}_1 = 3dx/R_0 = \text{Cn}_2$, $\beta'_1 = 0.075 = \beta'_2$, $M_1 = 10^{-3} = M_2$, $\sigma_1 = 1 = \sigma_2$.

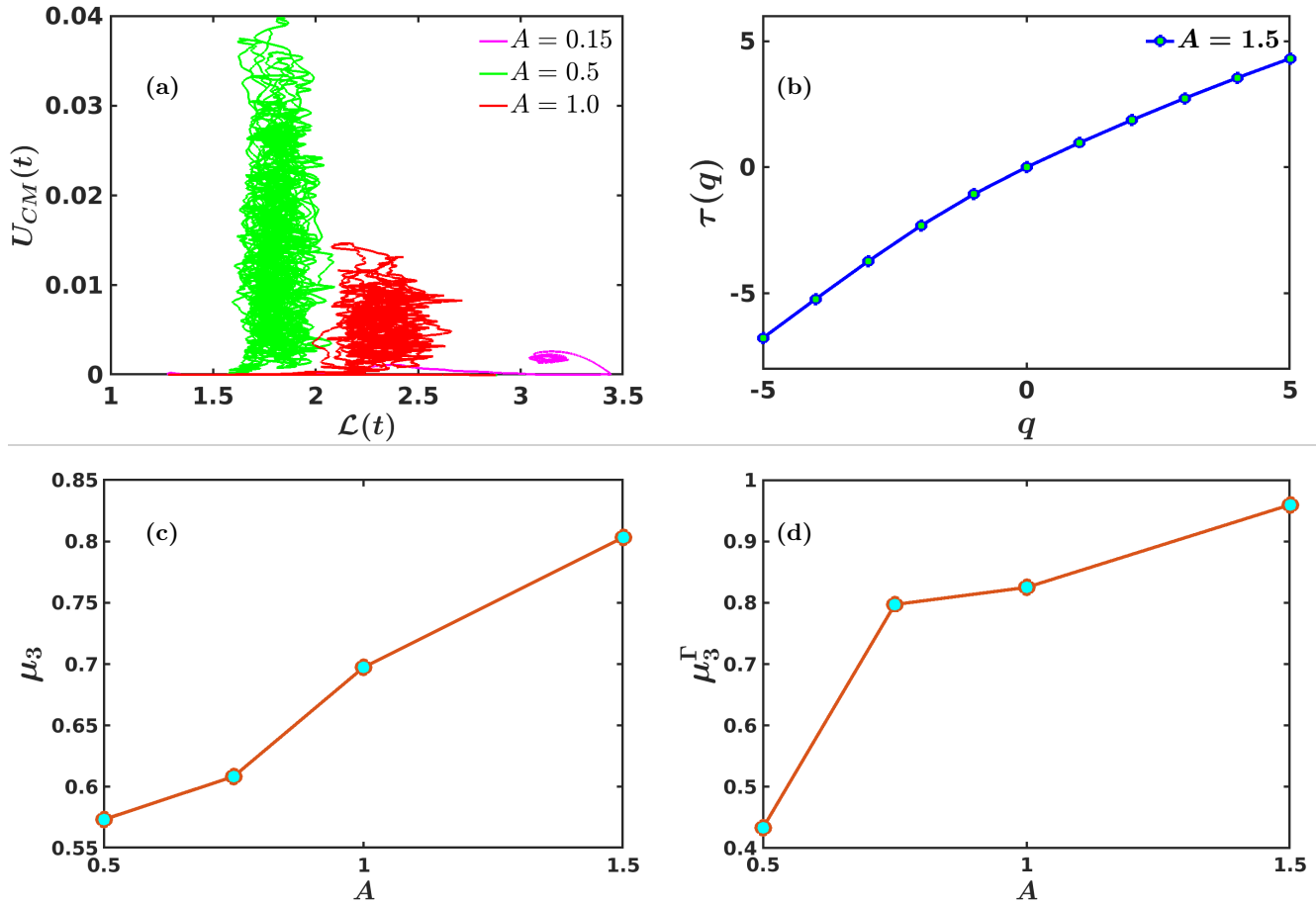


FIG. 4. (a) For $A = 0.15$, the system shows oscillatory behavior; this is confirmed by phase-space trajectories settling onto a limit cycle (the projection in the $U_{CM} - \mathcal{L}$ plane is shown via the illustrative magenta trajectory); as the system becomes turbulent, these trajectories become chaotic (see, e.g., the representative trajectories for $A = 0.5$ (green) and $A = 1$ (red)). (b) Plot of the generalized exponent $\tau(q)$ as a function of the order q for the representative value $A = 1.5$; the deviation from the linearity suggests the multifractality of $\Gamma(t)$. Plots versus A of (c) the skewness μ_3 of the PDFs of $U_{CM}(t)$ and (d) the skewness μ_3^Γ of the PDFs of $\Gamma(t)$.

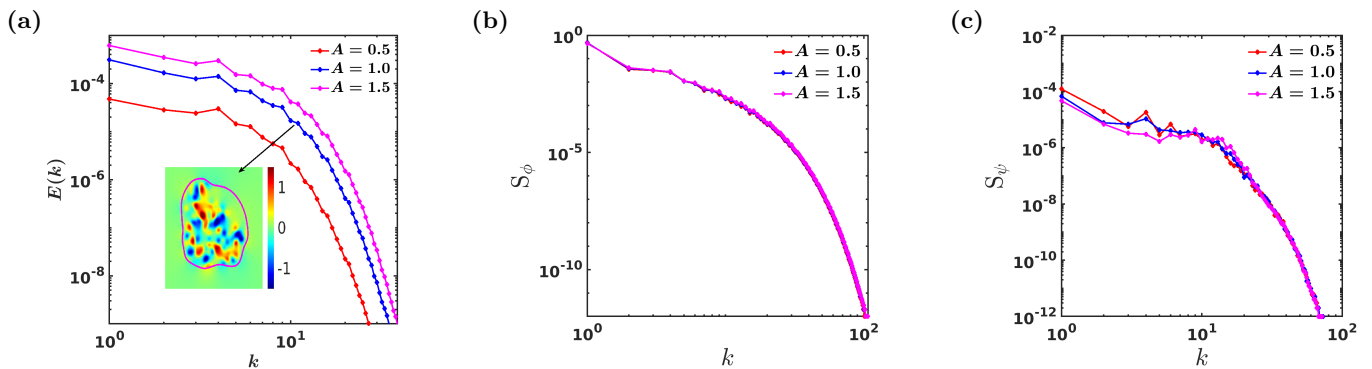


FIG. 5. Log-log plots versus the wave number k of the spectra (a) $E(k)$, (b) $S_\phi(k, t)$, and (c) $S_\psi(k, t)$ [Eq.10 in the main text], averaged over time in the statistically steady state, for $A = 0.5$ (red curves), $A = 1$ (blue curves), and $A = 1.5$ (magenta curves); the inset in (a) shows a representative pseudocolor plot of the vorticity field for $A = 1$.

Appendix C: Multifractal analysis

We use the wavelet-leader technique [42, 43] to obtain the multifractal spectrum of the Hurst exponents for the time series $\Gamma(t)$; we employ *MATLAB* [49] to perform this multifractal analysis. The wavelet leader $T_\psi[f](t, a)$ is obtained from the convolution operation for a time series $f(t)$ as follows:

$$T_\chi[f](t, a) = \frac{1}{a} \int_{-\infty}^{+\infty} \chi\left(\frac{t-b}{a}\right) f(t) dt. \quad (\text{C1})$$

Here, $\chi(t)$ is the form for a single wavelet, with a and b the scale and translation parameters, respectively. The structure function of order q , based on this wavelet leader, is

$$S_T(q, a) = \frac{1}{N_w} \sum_{i=1}^{N_w} |T_\chi[f](t, a)|^q \sim a^{\tau(q)}, \quad (\text{C2})$$

with $N_w = n/a$ the number of wavelets for a particular scale a and n the length of the entire time series. The Legendre transform of the generalized exponents $\tau(q)$ gives an upper bound for the generalized dimensions $D(h)$:

$$D(h) \leq \min_{q \neq 0} [1 + qh(q) - \tau(q)], \quad (\text{C3})$$

where $h(q) \equiv d\tau(q)/dq$ is the Hölder exponent of order q . For a monofractal time series, $\tau(q)$ is a linear function of q , so h is independent of q and $D(h)$ is nonzero for only this value of h . By contrast, for a multifractal time series, $\tau(q)$ is a nonlinear function of q [Fig. 4(b)] and $D(h)$ is a nontrivial function of h (see the main paper).

Appendix D: Calculation of the droplet's center-of-mass (CM)

The Fourier transform of the field $\phi(x, y)$ is

$$\hat{\phi}(k_x, k_y) = \sum_{(x,y)} \phi(x, y) \exp^{i(k_x x + k_y y)}. \quad (\text{D1})$$

The two components of the position of the droplet's CM can now be calculated as follows [39]:

$$\begin{aligned} X_{CM} &= \arctan\left(\Im(\hat{\phi}(1, 0)), \Re(\hat{\phi}(1, 0))\right); \\ Y_{CM} &= \arctan\left(\Im(\hat{\phi}(0, 1)), \Re(\hat{\phi}(0, 1))\right). \end{aligned} \quad (\text{D2})$$

Appendix E: Videos

The following videos are available on request; please send an email to nadia@iisc.ac.in and rahul@iisc.ac.in.

1. Video V1: Video showing the spatiotemporal evolution of the pseudocolor plots in Fig. 1 of the main text (row (a) for $A = 0$) and illustrating that, when $A = 0$, the domain growth of the ψ -field is driven purely by diffusion.
2. Video V2: Video showing the spatiotemporal evolution of the pseudocolor plots in Fig. 1 of the main text (row (b) for $A = 0.15$).
3. Video V3: Video showing the spatiotemporal evolution of vector plots of the velocity field \mathbf{u} , with the $\phi = 0$ contour line (magenta), overlaid on a pseudocolor plot of the vorticity ω normalised by its maximal value (cf. Fig. 1 of the main text (row (c) for $A = 0.15$)); the lengths of the velocity vectors are proportional to their magnitudes.
4. Video V4: Video showing the spatiotemporal evolution of the pseudocolor plots in Fig. 1 of the main text (row (d) for $A = 1$).

[1] S. Ramaswamy, *Journal of Statistical Mechanics: Theory and Experiment* **2017**, 054002 (2017).

[2] M. J. Bowick, N. Fakhri, M. C. Marchetti, and S. Ra-

- maswamy, *Physical Review X* **12**, 010501 (2022).
- [3] M. C. Marchetti, J.-F. Joanny, S. Ramaswamy, T. B. Liverpool, J. Prost, M. Rao, and R. A. Simha, *Reviews of modern physics* **85**, 1143 (2013).
- [4] B. Mahault, *Outstanding problems in the statistical physics of active matter*, Ph.D. thesis, Universite Paris-Saclay (2018).
- [5] C. Castellano, S. Fortunato, and V. Loreto, *Reviews of modern physics* **81**, 591 (2009).
- [6] A. Bottinelli, D. T. Sumpter, and J. L. Silverberg, *Physical review letters* **117**, 228301 (2016).
- [7] C. Becco, N. Vandewalle, J. Delcourt, and P. Poncin, *Physica A: Statistical Mechanics and its Applications* **367**, 487 (2006).
- [8] W. Bialek, A. Cavagna, I. Giardina, T. Mora, E. Silvestri, M. Viale, and A. M. Walczak, *Proceedings of the National Academy of Sciences* **109**, 4786 (2012).
- [9] A. Cavagna, A. Cimorelli, I. Giardina, G. Parisi, R. Santagati, F. Stefanini, and M. Viale, *Proceedings of the National Academy of Sciences* **107**, 11865 (2010).
- [10] C. Chen, S. Liu, X.-q. Shi, H. Chate, and Y. Wu, *Nature* **542**, 210 (2017).
- [11] R. Wittkowski, A. Tiribocchi, J. Stenhammar, R. J. Allen, D. Marenduzzo, and M. E. Cates, *Nature communications* **5**, 1 (2014).
- [12] M. E. Cates and J. Tailleur, *Annu. Rev. Condens. Matter Phys.* **6**, 219 (2015).
- [13] G. Gonnella, D. Marenduzzo, A. Suma, and A. Tiribocchi, *Comptes Rendus Physique* **16**, 316 (2015).
- [14] H. Wioland, F. G. Woodhouse, J. Dunkel, J. O. Kessler, and R. E. Goldstein, *Physical review letters* **110**, 268102 (2013).
- [15] D. Huang, Y. Du, H. Jiang, and Z. Hou, *Physical Review E* **104**, 034606 (2021).
- [16] G. Ramos, M. L. Cordero, and R. Soto, *Soft Matter* **16**, 1359 (2020).
- [17] G. Kokot, H. A. Faizi, G. E. Pradillo, A. Snezhko, and P. M. Vlahovska, *Communications Physics* **5**, 1 (2022).
- [18] A. Sokolov, L. D. Rubio, J. F. Brady, and I. S. Aranson, *Nature communications* **9**, 1 (2018).
- [19] T. Gao and Z. Li, *Physical Review Letters* **119**, 108002 (2017).
- [20] S. Copar, J. Aplinc, Z. Kos, S. Zumer, and M. Ravnik, *Physical Review X* **9**, 031051 (2019).
- [21] E. Tjhung, D. Marenduzzo, and M. E. Cates, *Proceedings of the National Academy of Sciences* **109**, 12381 (2012).
- [22] G. De Magistris, A. Tiribocchi, C. Whitfield, R. Hawkins, M. Cates, and D. Marenduzzo, *Soft Matter* **10**, 7826 (2014).
- [23] C. A. Whitfield, D. Marenduzzo, R. Voituriez, and R. J. Hawkins, *The European Physical Journal E* **37**, 1 (2014).
- [24] N. Yoshinaga, *The Journal of Chemical Physics* **150**, 184904 (2019).
- [25] L. J. Ruske and J. M. Yeomans, *Physical Review X* **11**, 021001 (2021).
- [26] F. Fadda, G. Gonnella, A. Lamura, and A. Tiribocchi, *The European Physical Journal E* **40**, 1 (2017).
- [27] R. Singh, E. Tjhung, and M. E. Cates, *Physical Review Research* **2**, 032024 (2020).
- [28] J. M. Yeomans, D. O. Pushkin, and H. Shum, *The European Physical Journal Special Topics* **223**, 1771 (2014).
- [29] A. A. Fragkopoulos, J. Vachier, J. Frey, F.-M. Le Menn, M. G. Mazza, M. Wilczek, D. Zwicker, and O. Baumbach, *Journal of the Royal Society Interface* **18**, 20210553 (2021).
- [30] N. Pal, P. Perlekar, A. Gupta, and R. Pandit, *Physical Review E* **93**, 063115 (2016).
- [31] P. Perlekar, N. Pal, and R. Pandit, *Scientific Reports* **7**, 1 (2017).
- [32] A. Tiribocchi, R. Wittkowski, D. Marenduzzo, and M. E. Cates, *Physical review letters* **115**, 188302 (2015).
- [33] M. R. Shaebani, A. Wysocki, R. G. Winkler, G. Gompfer, and H. Rieger, *Nature Reviews Physics* **2**, 181 (2020).
- [34] The active-matter terminology and the conventional fluid-dynamics nomenclature are slightly different. In the fluid-dynamics sense, both ϕ and ψ are active scalars insofar as they affect the velocity field \mathbf{u} . However, in the active-matter sense, ψ is active but ϕ is not.
- [35] C. Canuto, M. Y. Hussaini, A. Quarteroni, A. Thomas Jr, *et al.*, *Spectral methods in fluid dynamics* (Springer Science Business Media, 2012).
- [36] S. M. Cox and P. C. Matthews, *Journal of Computational Physics* **176**, 430 (2002).
- [37] P. G. Moerman, P. C. Hohenberg, E. Vanden-Eijnden, and J. Brujic, *Proceedings of the National Academy of Sciences* **115**, 3599 (2018).
- [38] We have checked explicitly that the precise direction of droplet propulsion depends on the realization of the random distribution of $\psi_0(\mathbf{x})$ in the initial condition.
- [39] L. Bai and D. Breen, *Journal of Graphics Tools* **13**, 53 (2008).
- [40] D. Elhmaidid, A. Provenzale, and A. Babiano, *Journal of Fluid Mechanics* **257**, 533 (1993).
- [41] S. Mukherjee, R. K. Singh, M. James, and S. S. Ray, *Physical Review Letters* **127**, 118001 (2021).
- [42] S. Jaffard, B. Lashermes, and P. Abry, in *Wavelet analysis and applications* (Springer, 2006) pp. 201–246.
- [43] H. Wendt and P. Abry, *IEEE Transactions on Signal Processing* **55**, 4811 (2007).
- [44] N. Padhan, K. Kiran, and R. Pandit, to be published.
- [45] R. Alert, J. Casademunt, and J.-F. Joanny, *Annual Review of Condensed Matter Physics* **13**, 143 (2022).
- [46] K. V. Kiran, A. Gupta, A. K. Verma, and R. Pandit, arXiv preprint arXiv:2201.12722 (2022).
- [47] A. Groisman and V. Steinberg, *Nature* **405**, 53 (2000).
- [48] A. Gupta and R. Pandit, *Physical Review E* **95**, 033119 (2017).
- [49] Multifractal analysis, https://in.mathworks.com/help/wavelet/ug/multifractal-analysis.html?s_tid=mwa_osa_a (2016-2020).